

Quantum reactive scattering calculations of cross sections and rate constants for the $\text{N}(^2D) + \text{O}_2(X^3\Sigma_g^-) \rightarrow \text{O}(^3P) + \text{NO}(X^2\Pi)$ reaction

Irene Miquel, Miguel González,^{a)} and R. Sayós

Departament de Química Física i Centre de Recerca en Química Teòrica, Universitat de Barcelona, C/Martí i Franquès, 1, 08028 Barcelona, Spain

Gabriel G. Balint-Kurti^{b)}

School of Chemistry, Centre for Computational Chemistry, The University of Bristol, Bristol BS8 1TS, United Kingdom

Stephen K. Gray^{c)}

Chemistry Division, Argonne National Laboratory, Argonne, Illinois 60439-4831

Evelyn M. Goldfield^{d)}

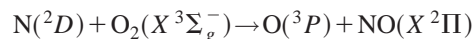
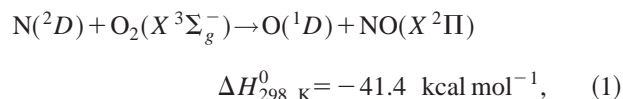
Department of Chemistry, Wayne State University, Detroit, Michigan 48202

(Received 4 September 2002; accepted 28 October 2002)

Time-dependent quantum wave packet calculations have been performed on the two lowest adiabatic potential energy surfaces ($2^2A'$ and $1^2A''$) for the $\text{N}(^2D) + \text{O}_2(X^3\Sigma_g^-) \rightarrow \text{O}(^3P) + \text{NO}(X^2\Pi)$ reaction. The calculations have been carried out, on these recently published potential energy surfaces, using the real wave packet method together with a new dispersion fitted finite difference technique for evaluating the action of the radial kinetic energy operator. Reaction probabilities, corresponding to the O_2 reactant in its ground vibrational-rotational state, have been calculated for both surfaces and for many different values of the total angular momentum quantum number (J), within the helicity decoupling approximation. The reaction probabilities associated with all other relevant J values have been interpolated, and to a smaller extent extrapolated, using a capture model, to yield probabilities as a function of energy. The probabilities have in turn been summed to yield energy dependent cross sections and then used to compute rate constants. These rate constants are compared with ones obtained from quasiclassical trajectory (QCT) and variational transition state theory (VTST) calculations performed on the same surfaces. There is a good agreement between the wave packet and QCT cross sections for reaction on both potential energy surfaces considered, with the exception of the near threshold region, where the reaction probability is dominated by tunnelling. Comparison of the predicted rate constants shows that for the $2^2A'$ surface, above 300 K, the wave packet, QCT and VTST results are quite similar. For the $1^2A''$ surface, however, significant differences occur between the wave packet and the other methods. These differences become smaller with increasing temperature. It is likely that these differences arise, at least in part, from the fact that, when calculating the rate constants, the reactants are restricted to be in their lowest vibrational-rotational state in the wave packet calculations but are selected from a thermally equilibrated population in the other methods. © 2003 American Institute of Physics. [DOI: 10.1063/1.1530575]

I. INTRODUCTION

The nitrogen atom in its first excited electronic state, $\text{N}(^2D)$, plays an important role in atmospheric chemistry.¹ The deactivation of $\text{N}(^2D)$ is mainly due to molecular oxygen in its ground electronic state, $\text{O}_2(X^3\Sigma_g^-)$, which reacts with it to produce vibrationally excited NO. This reaction can take place by means of two reactive channels,^{2,3}



$$\Delta H_{298\text{ K}}^0 = -86.7 \text{ kcal mol}^{-1}. \quad (2)$$

The thermal rate constant for the disappearance of $\text{N}(^2D)$ has been measured experimentally in a range of temperatures between 210 and 465 K. The overall rate includes contributions from both reactions (1) and (2) as well as from physical (i.e., nonreactive) electronic quenching.^{1,4} However, recent theoretical studies^{5–9} have clearly shown that reaction (2) is the dominant reactive process over a very wide temperature range, and have suggested (Refs. 6–9) that reaction (2) also dominates over the physical electronic quenching of $\text{N}(^2D)$ by O_2 . Thus, the experimentally measured rate constant probably arises mainly from reaction (2). The recommended expression for the temperature dependence of the

^{a)}Electronic mail: miguel@qf.ub.es

^{b)}Electronic mail: Gabriel.Balint-Kurti@Bristol.ac.uk

^{c)}Electronic mail: gray@anchim.chm.anl.gov

^{d)}Electronic mail: evi@sun.science.wayne.edu

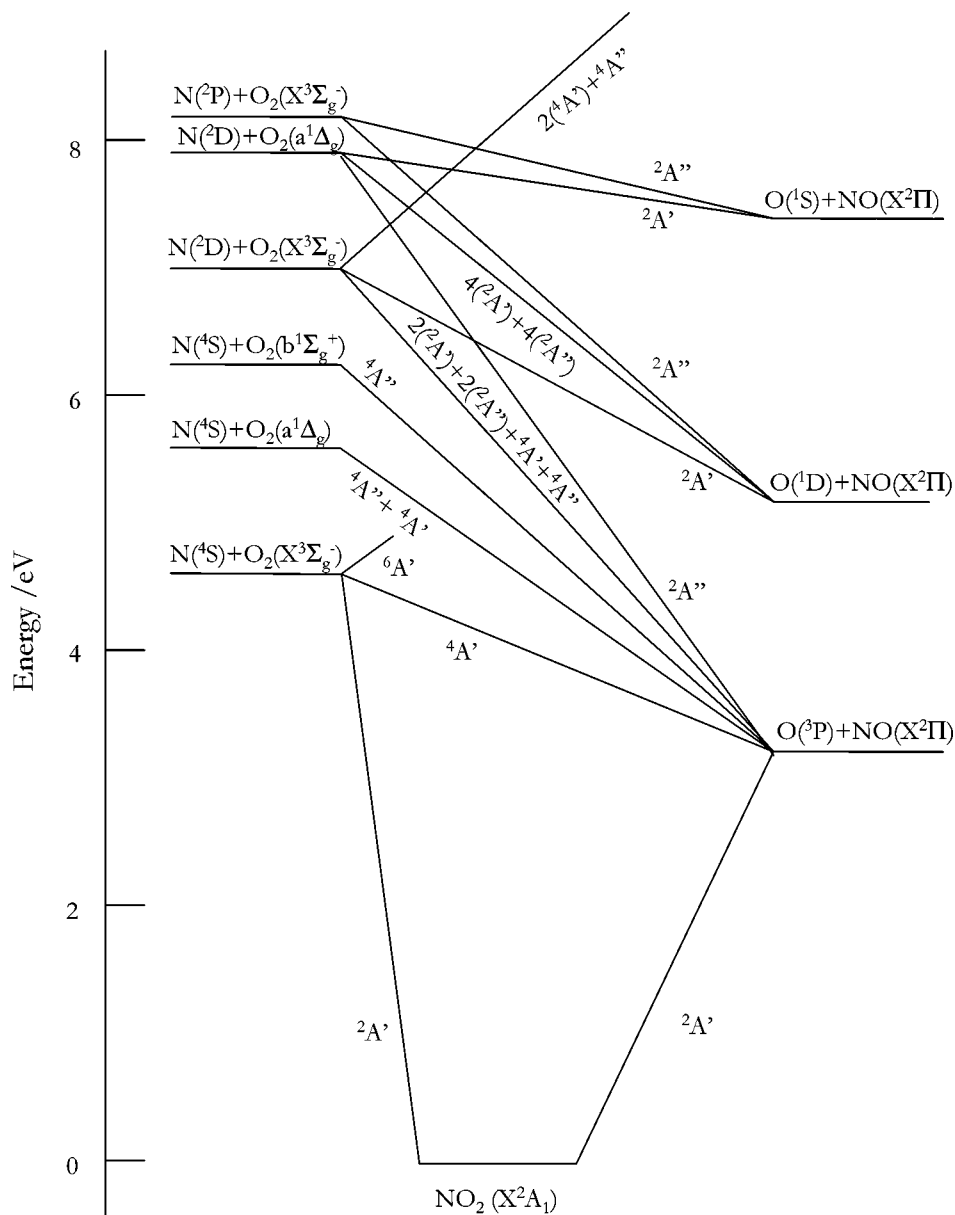


FIG. 1. Adiabatic correlation diagram connecting the electronic states of reactants ($\text{N}+\text{O}_2$) with those of products ($\text{NO}+\text{O}$). The numbers preceding the brackets, e.g., $2(^2A')$, indicate that there are two different states of the specified symmetry correlating between the two asymptotic limits.

rate constant¹⁰ (based on the data of Refs. 1 and 4) is $k = 9.7 \times 10^{-12} \exp(-185/T) \text{ cm}^3 \text{ molecule}^{-1} \text{ s}^{-1}$ in the temperature range of 210–465 K. As far as we know, only one experimental study¹¹ has been published in which the NO product vibrational population resulting from the $\text{N}(^2D) + \text{O}_2$ reaction has been reported. This study shows that, at 100 K, the NO product vibrational distribution is inverted and peaks at $v' = 7$.

Figure 1 presents an adiabatic electronic correlation diagram connecting $\text{N}+\text{O}_2$ reactants and $\text{NO}+\text{O}$ products.¹² There have been many theoretical studies of the lowest $^2A'$ potential energy surface (PES), which correlates with the ground state $\text{N}(^4S) + \text{O}_2(X^3\Sigma_g^-)$ reactants.^{13–19} In the current work we address exclusively the dynamics on the adiabatic PESs associated with reactions (1) and (2). There are six potential energy surfaces which correlate adiabatically from $\text{N}(^2D) + \text{O}_2(X^3\Sigma_g^-)$ reactants to $\text{O}(^3P) + \text{NO}(X^2\Pi)$ products, and a single potential energy surface which correlates from $\text{N}(^2D) + \text{O}_2(X^3\Sigma_g^-)$ reactants to $\text{O}(^1D)$

+ $\text{NO}(X^2\Pi)$ products. Several theoretical studies^{5–9} of reaction (2) have already been published in which analytical fits to *ab initio* calculations of adiabatic potential energy surfaces have been employed to calculate rate constants and vibrational distributions of products. These studies have used the variational transition state theory (VTST) and quasiclassical trajectory (QCT) methods to solve the necessary reaction dynamics. The theoretical study of reaction (2) is quite complicated because of the six potential energy surfaces ($2^2A'$, $3^2A'$, $1^2A''$, $2^2A''$, $3^4A'$, and $3^4A''$) that correlate reactants and products. However, only two of them ($2^2A'$ and $1^2A''$) possess sufficiently low energy barriers (0.08 and 0.25 kcal mol⁻¹, respectively, at the CASPT2/cc-pVTZ *ab initio* level^{7,8}) to permit reaction to take place at low temperatures or collision energies.

In two recent studies,^{7,8} high level *ab initio* calculations were carried out for the $2^2A'$ and $1^2A''$ surfaces of reaction (2). More than 500 *ab initio* points for each of the two lowest surfaces were computed and fitted to an analytic Sorbie–

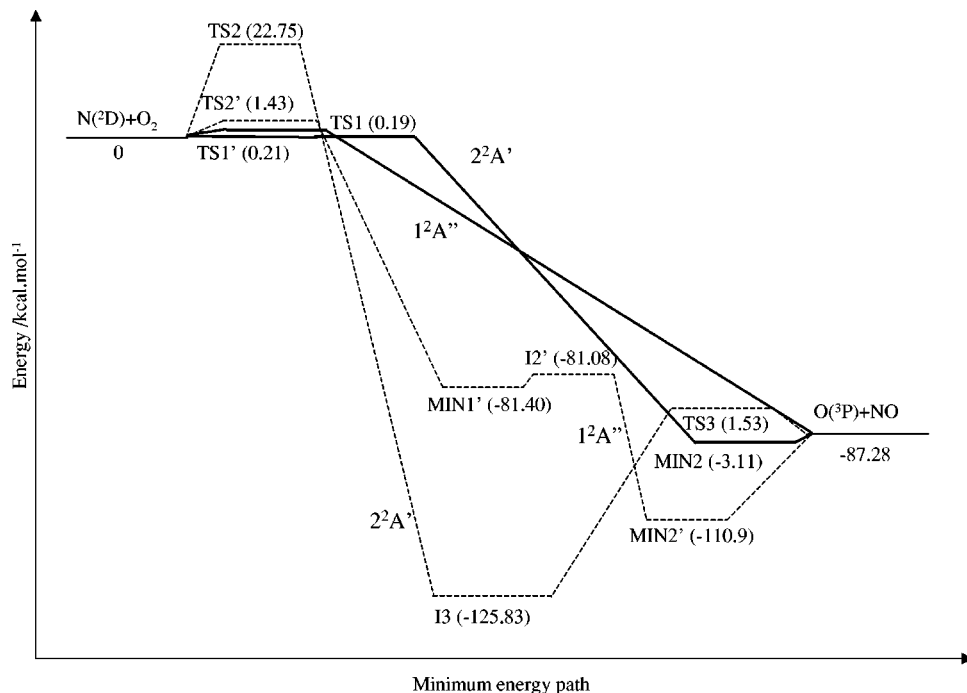


FIG. 2. Energetics of minimum energy paths for the reaction $N(^2D) + O_2(X^3\Sigma_g^-) \rightarrow O(^3P) + NO(X^2\Pi)$ computed on the two lowest adiabatic potential energy surfaces, $2^2A'$ and $1^2A''$. The solid lines correspond to the minimum energy pathways for abstraction and the dashed lines for insertion. The energies are given in kcal mol^{-1} and do not include zero point energy contributions. The unprimed symbols (i.e., TS1, TS2, etc.) correspond to the $2^2A'$ surface while the primed symbols (i.e., TS1', TS2', etc.) correspond to the $1^2A''$ surface.

Murrell many-body functional form.^{20,21} Moreover, some kinetic and dynamic properties of the reaction were calculated using the VTST and QCT methods. In the present paper we report the first three-dimensional quantum dynamics study of the $N(^2D) + O_2(X^3\Sigma_g^-) \rightarrow O(^3P) + NO(X^2\Pi)$ reaction on these two potential energy surfaces. We investigate the possibility of interesting quantum effects and compare accurate quantum mechanical predictions with those of statistical and quasiclassical trajectory theories. By performing a limited number of quantum mechanical reactive scattering calculations for a range of total angular momentum values, and by using capture model techniques to interpolate and extrapolate these results to obtain estimates of reaction probabilities for all other relevant values of the total angular momentum, we are able to estimate reactive cross sections and thermal rate constants. These are compared with QCT, VTST, and experimental values.

Salient aspects of the potential energy surfaces, which have been previously reported, are briefly summarized in Sec. II. The wave packet formalism is described in Sec. III and our results are presented in Sec. IV. A summary of the main conclusions of the work is given in Sec. V.

II. POTENTIAL ENERGY SURFACES

The lowest potential energy surface which correlates adiabatically between reactants and products for reaction (2) is the $2^2A'$ PES.^{6,7} The reaction is exothermic by 3.76 eV and the analytical representation of the surface has a very small energy barrier⁷ [0.013 eV (0.30 kcal mol^{-1}) taking into account the zero point energy (ZPE)] for the reaction to occur via the abstraction pathway. Figure 2 shows schematic energy profiles along the minimum energy paths (MEPs) for the analytical PESs for both the $2^2A'$ and $1^2A''$ states. Two reaction pathways are possible, abstraction and insertion, on both surfaces, and the energetics along both pathways is

shown. The transition state (TS) for abstraction on the $2^2A'$ PES (TS1 on Fig. 2) has C_s symmetry with a NOO angle of 120.47° . There are also two van der Waals (vdW) minima located respectively in the entrance and exit channels along the MEP.⁷ The lowest energy route to the insertion [perpendicular approach of the $N(^2D)$ atom to the middle of the O_2 molecule (C_{2v} symmetry)] has a TS, TS2 on Fig. 2, which lies 0.98 eV (22.75 kcal mol^{-1}) above the energy of the reactants.⁷ The energies quoted do not include the effect of ZPE. The TS for the insertion pathway (TS2) is a second order saddle point. Because of the high energy of TS2, the insertion pathway cannot, in principle, really be accessed at the energies considered in the present paper. The shape of the MEP along this insertion pathway is more complicated than that of the abstraction pathway, due to the existence of three intersections between the ground $1^2A''$ and the $2^2A'$ surfaces.²² The last one of these intersections has a peaked topology and is located between two NO_2 minima [$NO_2(X^2A_1)$ and $NO_2(^2B_2)$], with the lowest energy point of the intersection seam being located 2.14 eV below the products.²²

The second lowest adiabatic potential energy surface for reaction (2) is the $1^2A''$ PES.^{6,8} This surface can again lead to reaction through an abstraction or an insertion pathway⁸ as with the $2^2A'$ surface, but in contrast to this latter surface there is a very small energy barrier to reaction via either of the two mechanisms in this case (see Fig. 2, TS1' and TS2'). The TS corresponding to the abstraction path (TS1') on the $1^2A''$ analytical PES is associated with a barrier⁸ of only 0.013 eV (0.30 kcal mol^{-1}) including the ZPE, and its geometry is very similar to the abstraction TS on the $2^2A'$ PES, having a geometry corresponding to a NOO angle of 109.30° (note that the height of this barrier is identical to that on the $2^2A'$ PES when ZPE is taken into account). The energy barrier to the insertion reaction on the $1^2A''$ analytical PES

is 0.050 eV (1.15 kcal mol⁻¹) including the ZPE (in the analytical PES this TS corresponds to a second order saddle point). As in the case of the insertion pathway on the 2²A' PES, the topology of the reaction coordinate for the insertion on the 1²A'' PES is complex, involving three intersections along the C_{2v} minimum energy path.⁸

III. QUANTUM REACTIVE SCATTERING METHOD

A. Time-dependent real wave packet approach

The time-dependent real wave packet method, developed by Gray and Balint-Kurti,²³ has been used in the present work to obtain total reaction probabilities at different values of the total angular momentum quantum number (*J*). As the system consists of three heavy, i.e., nonhydrogenic, atoms we have had to use small radial and angular grid spacings. The main advantage of this method is that only the real part of the wave packet is propagated, thus both computation time and computer memory are significantly reduced. In order to ensure that the computational time required was minimized, we have also used the dispersion fitted finite difference method developed by Gray and Goldfield²⁴ to evaluate the action of the radial differential operators on the wave packet.

Two possible coordinate systems can be used to propagate the wavepacket: a reactant coordinate system or a product coordinate system.²⁵ We can use reactant coordinates to calculate total reaction probabilities, but must use product coordinates if we wish to compute product state distributions or state-to-state reaction probabilities. In this work we will compute only total reaction probabilities and cross sections and will therefore use reactant Jacobi coordinates. For the N(²D)+O₂→O(³P)+NO system, the reactant Jacobi coordinates are denoted by *R*, *r*, and *γ*, where *R* is the N(²D)-O₂ center of mass distance, *r* is the O-O internuclear distance, and *γ* is the angle between the vectors **R** and **r**.

In the real wave packet approach the wave function evolves under a modified time-dependent Schrödinger equation,

$$i\hbar \frac{\partial \psi(x,t)}{\partial t} = f(\hat{\mathbf{H}}) \psi(x,t), \quad (3)$$

where *x* denotes all coordinates (*R*, *r*, *γ*) and the Hamiltonian has been replaced by a function of itself,

$$f(\hat{\mathbf{H}}) = -\frac{\hbar}{\tau} \cos^{-1}(\hat{\mathbf{H}}_s). \quad (4)$$

$\hat{H}_s = a_s \hat{H} + b_s$ is the scaled and shifted Hamiltonian with *a_s* and *b_s* chosen in such a way that the maximum and minimum eigenvalues of \hat{H} lie in the interval (-1,1). This scaling ensures a single valued mapping. The propagation is more efficient if the energy range of the Hamiltonian is as small as possible and so a maximum value or a cut-off energy, *V_{cut}*, has been introduced and it is applied to the potential to reduce the energy range. The propagation of the wave packet is achieved by a Chebyshev iteration where each step requires only a single evaluation of the action of the Hamiltonian on a real vector. A grid representation is used for the wave packet and the potential. The *R* and *r* grids are taken to be

evenly spaced. The angular part of the wave function is represented using a grid or discrete variable representation (DVR) (Refs. 26, 27) based on Gauss-Legendre quadrature points. The potential matrix is diagonal in this representation. In this work, the evaluation of the kinetic energy term associated with *R* and *r* is not accomplished using fast Fourier transforms as in previous studies,^{28,29} but with the dispersion fitted finite difference method recently developed by Gray and Goldfield.²⁴ This results in a significant reduction of computation time.

Let ψ be the representation of the wavepacket on a discrete grid of points and let *q* and *p* denote the real and imaginary parts of the wave packet, respectively, i.e., $q = \text{Re}\{\psi\}$ and $p = \text{Im}\{\psi\}$, then the central equation of our approach, is

$$q_{k+1} = \hat{\mathbf{A}}(-\hat{\mathbf{A}}q_{k-1} + 2\hat{\mathbf{H}}_s q_k), \quad (5)$$

where *k* denotes the iteration step, *k*=1,...,*N*. The recursion, Eq. (5), was originally introduced by Mandelshtam and Taylor in the context of a time-independent Green's function approach.^{30,31} The real wave packet²³ method can be thought of as a more explicitly time-dependent interpretation of this work and also of the time-independent wave packet ideas of Kouri and co-workers.^{32,33}

When finite grids are used the wave packet has to be absorbed to prevent it from reaching the end of the grid. $\hat{\mathbf{A}}$ is some appropriate operator, which damps the wave packet amplitude as it approaches the grid edges.^{34,35} Let *q₀* be the real part and *p₀* the imaginary part of the initial wave packet $\psi(R, r, \gamma, t=0)$. The recursion Eq. (5) requires *q₀* and *q₁* to be initialized. In the present case the initial condition is complex and the initial step in the iteration process to evaluate *q₁* is

$$q_1 = \hat{\mathbf{A}}[\hat{\mathbf{H}}_s q_0 - \sqrt{1 - \hat{\mathbf{H}}_s^2} p_0]. \quad (6)$$

The square root is evaluated with a Chebyshev series expansion.³⁶

The initial wave packet used in the calculation is chosen to be

$$\begin{aligned} \psi(R, r, \gamma, t=0) = & N \exp[-\alpha(R-R_0)^2] \\ & \times \exp[-ik_0(R-R_0)] \chi_{vj}(r) \phi_j(\cos \gamma), \end{aligned} \quad (7)$$

where $\chi_{vj}(r)$ is the initial vibrational wave function of the O₂ reactant and $\phi_j(\cos \gamma)$ its initial rotational state. $\exp[-ik_0(R-R_0)]$ is a phase factor which gives the wave packet a relative momentum of $k_0\hbar$, associated with a relative kinetic energy of $E_{\text{trans}} = (\hbar k)^2/2\mu$, towards the interaction region. $N \exp[-\alpha(R-R_0)^2]$ is a normalized Gaussian function centered on the N-O₂ scattering distance $R=R_0$. In these calculations the O₂ is considered to be initially in its ground vibrotational state (*v*=0, *j*=0). The wave packet is analyzed by determining the flux³⁷ passing, in the positive *r* direction, through a line drawn at some large fixed value of $r(r=r^*)$. The value of r^* should be sufficiently large to ensure that the initial reactant bond has been broken and that reaction has taken place, but it is important to note that r^* need not be in the asymptotic region of the potential.

B. Capture model approach

The integral reactive cross section summed over all final quantum states for a reactive scattering process is given by^{38,39}

$$\sigma_{\text{all} \leftarrow v, j}^{\text{tot}} = \frac{\pi}{k_{vj}^2} \sum_J \frac{(2J+1)}{(2j+1)} \sum_{v'} \sum_{j'} \sum_{\lambda \lambda'} |S_{v'j'\lambda' \leftarrow vj\lambda}^J|^2, \quad (8)$$

where $S_{v'j'\lambda' \leftarrow vj\lambda}^J$ are the state-to-state reactive scattering S matrix elements and there is one summation over the total angular momentum quantum number, J , and further summations over the helicity quantum numbers λ and λ' , which are the quantum numbers for the z component of the total angular momentum referred to the body-fixed coordinate system, as well as summations over v' and j' , the vibrational and rotational quantum numbers of the products. J is a good quantum number because the total angular momentum is a strictly conserved quantity and calculations can be carried out separately for each value of J . The helicity quantum numbers, λ and λ' , are not good quantum numbers, in the sense that the nuclear dynamics couples different λ values. In the present wave packet calculations the initial state of the O₂ is always $j=0$. In this case the initial value of λ must also be zero. The different λ values are coupled by the centrifugal coupling terms in the Hamiltonian operator. For $J=0$, λ is also equal to zero and centrifugal terms in the Hamiltonian can be omitted. In the case of nonzero total angular momentum a separate wavepacket is required for each value of λ and these different wave packets are all coupled. Thus for J greater than zero, in an exact treatment, it is necessary to propagate $J+1$ or J coupled wave packets (depending on the parity) for each value of J . In this work helicity decoupled calculations have been carried⁴⁰ out in which λ is assumed to remain equal to zero throughout.

In order to compute a reactive cross section we need to solve the dynamics for many J values. Now let us define the total reaction probability P_{react}^J corresponding to a particular initial relative translational energy as

$$P_{\text{react}}^J = \frac{1}{(2j+1)} \sum_{v'} \sum_{j'} \sum_{\lambda \lambda'} |S_{v'j'\lambda' \leftarrow vj\lambda}^J|^2. \quad (9)$$

Substituting Eq. (9) into Eq. (8) we obtain

$$\sigma_{\text{all} \leftarrow v, j}^{\text{tot}} = \frac{\pi}{k_{vj}^2} \sum_J (2J+1) P_{\text{react}}^J. \quad (10)$$

To compute cross sections we must calculate the total reaction probability for all the values of J that contribute to the sum in Eq. (10). This computational problem may be simplified by using a “ J -shifting” approximation.^{40,41} In this type of approximation the reaction probability is calculated for a limited number of J values, or even just for $J=0$, and approximate methods are used to estimate the reaction probability for other required J values from those for which more accurate calculations have been performed. J -shifting approximations rely on the identification of a “bottleneck” geometry, such as a transition state. The changes in rotational

energy of the system, when fixed at this geometry, provide an energy shift, E_{shift} , which is used in estimating the reaction probabilities,

$$P_{\text{react}}^J(E) = P_{\text{react}}^{J=0}(E - E_{\text{shift}}^J), \quad (11)$$

where $P_{\text{react}}^{J=0}(E)$ is the accurately computed reaction probability for $J=0$, at the total energy E , and $P_{\text{react}}^J(E)$ is the estimated reaction probability for another value of J .

The J -shifting method depends upon our ability to identify a unique bottleneck geometry. In the present case the barrier to reaction via the abstraction mechanism is very small on both PESs, while on the 1²A'' PES there are two distinct energetically accessible pathways to the reaction. For this reason we have chosen to use a related method, the capture model,^{40,42} which does not depend on the existence of a barrier to the reaction. In this approach the energy of the centrifugal barrier in an effective one-dimensional potential is used to define the energy shift needed in Eq. (11). For the case of $\lambda=0$, we define the one-dimensional effective potential as

$$V_J^{\text{eff}}(R) = \langle vj | V | vj \rangle + \frac{\hbar J(J+1)}{2\mu R^2}, \quad (12)$$

where $\langle vj | V | vj \rangle$ is the potential averaged over the initial vibrotational state of the reactants and is a function of the reactant scattering Jacobi coordinate. The effective potential exhibits a centrifugal barrier in the entrance channel. Let V_J^* be the height of the effective potential barrier corresponding to a total angular momentum quantum number J . In the capture model the reaction probability is now estimated as

$$P_{\text{react}}^J(E) = P_{\text{react}}^{J=0}(E - V_J^*). \quad (13)$$

Both in the J -shifting model and in the capture model it is assumed that the reaction probabilities are a function of the available energy, which is the energy in excess of the barrier height. This function of the excess energy is assumed to be universal (i.e., the same for all J values). One can then take the results for some particular J values and use them to define how reaction probability varies as a function of the excess energy.

In the present paper we compute the total reaction probability for many values of the total angular momentum J , and we use the capture model approach to interpolate between values of J for which we know the reaction probability. Suppose that we have calculated the reaction probability for J_1 and J_2 and that J lies between these two J values ($J_1 < J < J_2$). Then the reaction probability for J can be estimated as

$$P_{\text{react}}^J(E) = P_{\text{react}}^{J_1}(E - (V_J^* - V_{J_1}^*)) \frac{(J_2 - J)}{(J_2 - J_1)} + P_{\text{react}}^{J_2}(E + (V_J^* - V_{J_2}^*)) \frac{(J - J_1)}{(J_2 - J_1)}. \quad (14)$$

For the highest J values needed (up to $J=140$), where no wave packet calculations at higher values of J have been carried out, the reaction probability is extrapolated using the formula,

$$P_{\text{react}}^J(E) = P_{\text{react}}^{J_1}(E - (V_J^* - V_{J_1}^*)), \quad (15)$$

TABLE I. Grid and initial condition details for wave packet calculations.^a

Scattering coordinate (R) range	0–14.5
Number of grid points in R	392
Internal coordinate (r) range	0.5–6.5
Number of grid points in r	170
Number of angular basis functions	40
Absorption region length in R , r	1
Absorption strength (c_{abs})	0.05
Center of initial wave packet (R_0)	12.5
Width parameter of the wave packet, α	0.25
Initial relative translational energy/eV	0.05, 0.1, 0.25, 0.5
Cut-off energy, V_{cut} /eV	5.98

^aAll quantities are given in atomic units unless otherwise indicated.

where, in this case, J_1 is the highest value of J considered in the wave packet calculations.

C. Backward propagation method

The theory used to analyze the wave packet and to determine the reaction probability requires that the initial wave packet be placed in the asymptotic region, where there is very little interaction between the reactants.^{23,37} This is because we require knowledge of the amplitude of the initial wave packet associated with a given relative translational energy in this asymptotic region. For large values of the total angular momentum the centrifugal potential is very long ranged and it is in practice impossible to place the initial wave packet at sufficiently large separations so as to render the centrifugal potential unimportant. In order to overcome this problem and also to overcome problems arising from the intrinsically long range nature of the potential energy surfaces, we place the initial wave packet at a large but manageable separation of the reactants and after calculating an effective potential, as in Eq. (12), we propagate the R dependent part of the wave packet [see Eq. (7)] backwards in one dimension. We then analyze the backwards-propagated wave packet and use the resulting momentum distribution in the analysis of the final wave packet to yield the total reaction probability.²³

D. Calculation details

Calculations have been carried out on the two potential energy surfaces discussed in Sec. II above. Table I lists the details of the initial wave packet and the grids used in the calculations. Calculations were performed using the helicity decoupled method for total angular momentum quantum numbers $J=0, 5, 10, 20, 30, 40, 60, 80$, and 100. The initial wave packets were centered at a reactant scattering distance of 12.5 Bohr and, as described above, the momentum distribution of the initial wave packet was obtained using our *backward propagation* method, involving a one-dimensional backwards propagation of the initial wave packet. The calculations were performed using four different initial relative translational energies and the resulting reaction probabilities were combined to yield the total reaction probability over an extended energy range. Use was made of the exchange symmetry of the two oxygen atoms, so the 40 angular grid points used were equivalent to using reactant rotational states up to

$j=78$. The flux analysis method³⁷ was used to compute the total net outward flux through an analysis line that was located at a fixed value of the O–O vibrational coordinate (r^*) equal to 5.0 Bohr. From this we are able to compute the total reaction probability using standard formulas.

The damping operator, \hat{A} , used in Eq. (6) corresponds to the form $\hat{A}_R(R)\hat{A}_r(r)$, where the absorption functions used were $\hat{A}_x(x)=\exp[-c_{\text{abs}}(x-x_{\text{abs}})^2]$ for $x>x_{\text{abs}}$ and $\hat{A}_x=1$ otherwise with $x=R$ or r . This form is consistent with a quadratic imaginary absorbing potential.^{34,35} The calculations were run for 30 000 iteration steps which was sufficient to reach convergence. Each calculation required about 2 days of computational time on a single processor of a SGI R12000 based computer.

IV. RESULTS

A. Reaction probabilities

Figures 3(A) and 3(B) show the total reaction probabilities for the $\text{N}(^2D)+\text{O}_2(X^3\Sigma_g^-)\rightarrow\text{O}(^3P)+\text{NO}(X^2\Pi)$ reaction on the two surfaces, $2^2A'$ and $1^2A''$, respectively, for zero total angular momentum. The O_2 molecule is started in its lowest vibrational and rotational state ($v=0, j=0$). Each wave packet calculation yields reaction probabilities for a range of energies of about 0.25 eV. In order to provide results for a range of total energies between 0.1 and 0.8 eV, four calculations were therefore performed. The values of the relative translational energies of the initial wavepackets were centered on 0.05, 0.1, 0.25, and 0.5 eV. Figure 3(A) shows the total reaction probability on the lowest adiabatic surface for the reaction, i.e., the $2^2A'$ PES. The zero point energy of the O_2 diatomic is 0.0998 eV and the surface has a barrier to reaction of 0.013 eV if ZPE effects are included.⁷ The reaction probability starts to build up at 0.104 eV and by 0.113 eV, where we would expect to see the reaction threshold in the absence of tunnelling, it has reached a small, but non-negligible value (≈ 0.06).

The reaction probability for $J=0$ is seen, on average, to increase gradually from the threshold upwards [Fig. 3(A)]. This behavior should be contrasted to that of the $\text{O}(^1D)+\text{H}_2$ (Ref. 28) and $\text{O}(^1D)+\text{HCl}$ (Ref. 29) systems. These reactions are similar to the present one in that they are exothermic and display no, or very small, barriers to reaction. The total reaction probabilities for both these other systems however rise very rapidly, seemingly instantaneously, to a large value of near unity immediately above the threshold energy. The gradual rise in the present case is much more characteristic of a system with a barrier to reaction, as in the case of the excited $1^1A''$ PES for the $\text{O}(^1D)+\text{H}_2$ system.⁴² The behavior displayed in Fig. 3(A) may be due to the topology of the surface in the present case. The $2^2A'$ PES used in this work exhibits a quite high anisotropic behavior in comparison to the $1^1A''$ PES. That is to say, at values of the NOO angle different from that of the transition state on the $2^2A'$ PES (120.5°) the potential becomes much more repulsive (see Fig. 2 of Ref. 7) than in the case of the $1^1A''$ PES. This constriction of the reaction path may be expected to create a dynamical bottleneck similar to that arising from an energy barrier.

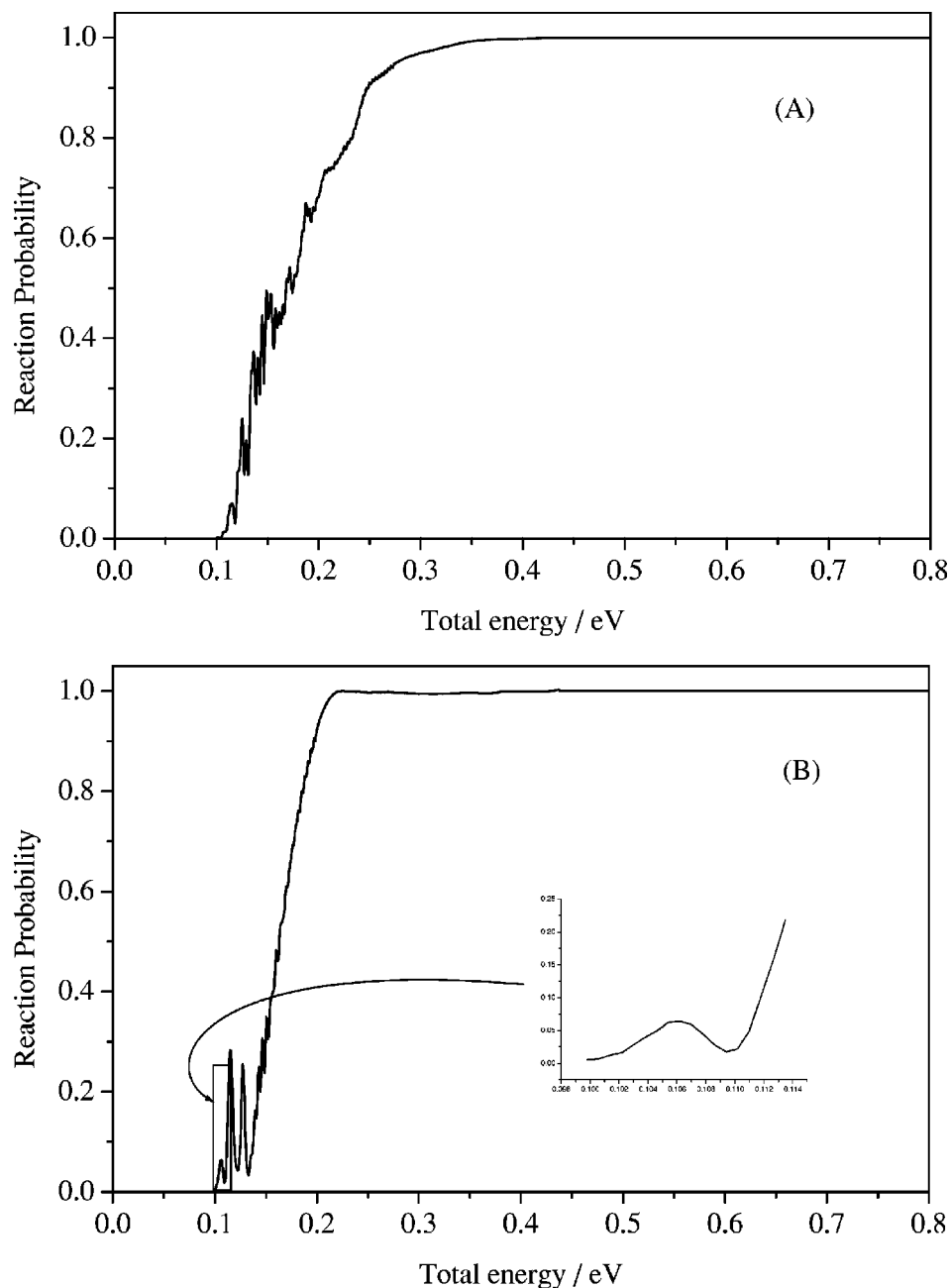


FIG. 3. Total reaction probabilities for $J=0$, calculated using the quantum wave packet method, plotted as a function of total energy for the reaction $N(^2D) + O_2(X^3\Sigma_g^-) \rightarrow O(^3P) + NO(X^2\Pi)$. The initial vibrational-rotational state of the O_2 reactant is $v=0, j=0$. The reaction probabilities were computed on the two lowest adiabatic potential energy surfaces (A) $2^2A'$ and (B) $1^2A''$. Note that the zero point energy of the O_2 reactant is 0.0998 eV.

At total energies above about 0.3 eV the total reaction probability for $J=0$ eventually attains a nearly constant value of unity, showing that there is no recrossing and all the collisions become reactive. This can be attributed to the large exothermicity of the reaction (3.76 eV) and the absence of long-lived collision complexes. There is however clear indication of resonance structure in the reaction probability at low collision energies. These could be due to reactive scattering resonances arising from quasibound bending vibrational states near the transition state in the entrance valley.

Figure 3(B) shows the total reaction probability for $J=0$ on the $1^2A''$ PES. The form of the reaction probability is qualitatively similar to that displayed for the $2^2A'$ surface [Fig. 3(A)]. There is somewhat more tunnelling for reaction on the $1^2A''$ PES than on the $2^2A'$ surface. This is shown in the inset in Fig. 3(B). The magnified portion corresponds to the energy range 0.1–0.113 eV. This is the energy range from

the zero point energy of O_2 up to the zero point vibrational energy of the very low transition state barrier for the abstraction reaction on the surface. It is interesting to observe that there appears to be a resonance in this tunnelling region. This is followed by two more well defined resonances and then a sharp rise in the reaction probability to unity. The rise of the reaction probability to near unit values is faster in this case, than on the $2^2A'$ surface. These results are consistent with the discussion above for the $2^2A'$ surface. The differences may be attributed to the fact that the insertion pathway is now available to the reaction, which was not the case for the $2^2A'$ surface. This would effectively make the $1^2A''$ surface less anisotropic so that, in line with the discussion presented above, it would present less of a dynamical bottleneck to reaction.

Reaction probabilities for values of J greater than zero

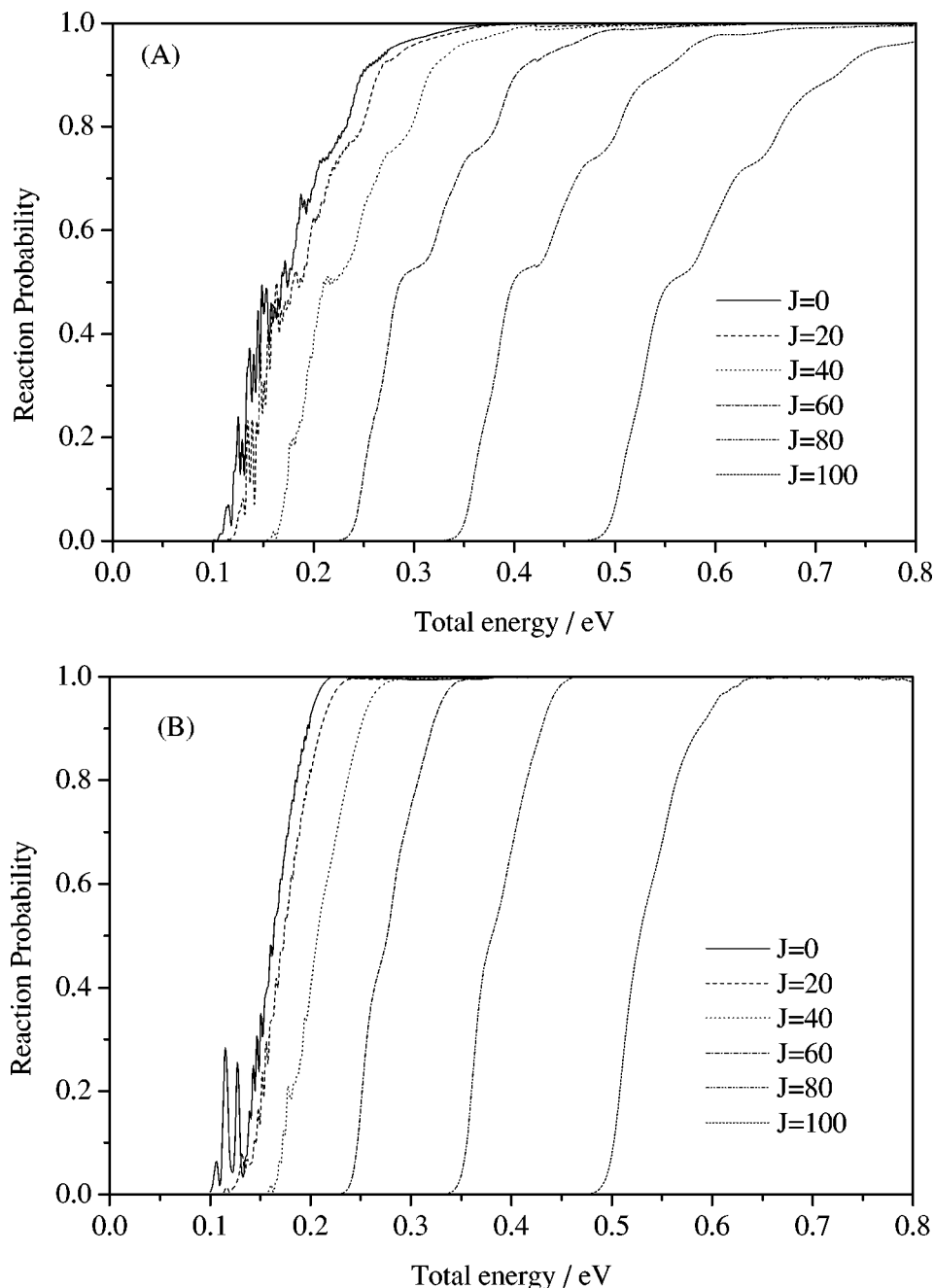


FIG. 4. Total reaction probabilities, calculated using the quantum wave packet method, for different values of J , plotted as a function of total energy for the reaction $\text{N}(^2D) + \text{O}_2(^3\Sigma_g^-) \rightarrow \text{O}(^3P) + \text{NO}(^2\Pi)$. The initial vibrational-rotational state of the O_2 reactant is $v=0, j=0$. The reaction probabilities were computed on the two lowest adiabatic potential energy surfaces (A) $2^2A'$ and (B) $1^2A''$.

are taken into account in the next subsection, in the context of the cross sections and rate constants calculations.

B. Cross sections and rate constants

To evaluate the total reactive cross section for reaction (2) from the ground vibrotational state of reactants [$\text{O}_2(v=0, j=0)$], several calculations at different non-zero values of the total angular momentum quantum number, J , were performed. The helicity-decoupling approximation in which λ is assumed to equal zero was used. The approximation is used here for practical reasons rather than because we are confident of its validity. The validity of this widely used approximation has recently been investigated.^{43,44} It is expected that it will be more valid for abstraction than for insertion reaction dynamics. The helicity-decoupled calculations

were carried out in reactants Jacobi coordinates and the J values employed are 0, 5, 10, 20, 30, 40, 60, 80, and 100. The maximum J value used depends on the energy for which the cross section is required, and is such that for higher J values the reaction probability is zero at the energy of interest. For reaction on the $2^2A'$ surface and for a maximum total energy of 0.8 eV the maximum required value of J used in the calculation of the reaction cross section was $J=140$.

Figure 4(A) shows the reaction probability evaluated on the $2^2A'$ surface for J values of 0, 20, 40, 60, 80, and 100. There are several interesting observations that may be made regarding this figure. First, as J increases the threshold for the reaction moves gradually to higher energies. This is a direct result of the presence of the centrifugal barrier, which prevents reaction when the reactants have insufficient energy

to approach each other. The second thing that is apparent from the figure is that as J increases the resonance structure present at low values of J gradually disappears. This would appear to be a real and interesting aspect of the reaction dynamics. Finally, as is clearly apparent from the reaction probabilities for higher values of J shown in the figure, the individual reaction probabilities does not in fact increase smoothly with increasing energy. They have a stepped structure. The underlying dynamical cause of this stepped structure is also of interest in interpreting the detailed dynamics of the reactive process. We speculate that this structure may be related to excitation of the bending motion near the abstraction transition state (TS1 in Fig. 2). The associated normal mode vibrational frequency is 198 cm^{-1} (see Ref. 7) and this approximately corresponds to the energy spacings between the major resonance structures in the low J reaction probability plots.

Figure 4(B) shows the reaction probability calculated on the $1^2A''$ surface for J values of 0, 20, 40, 60, 80, 100, and 120. The figure is qualitatively similar to Fig. 4(A). It again shows that the resonance structures, present for small J values, disappear for higher values of J . However, in the case of reaction on the $1^2A''$ surface the stepped structure of the rate of increase of the reaction probability with increasing energy is missing. This suggests that the underlying cause of this stepped structure probably lies in the angular dependence of the PESs and in the fact that for the $2^2A'$ surface the possibility of reaction is restricted to a more limited range of N–O–O angles.

Figures 5(A) and 5(B) present the total reactive cross section for reaction with O $_2$ ($v=0, j=0$) on the $2^2A'$ and $1^2A''$ PESs, evaluated with the help of the capture model approach, as a function of the initial relative translational energy. Figure 5(A) shows the total reactive cross section on the $2^2A'$ surface. The reactive cross section is seen to increase smoothly with relative translational energy and reaches a constant value at an energy of around 0.4 eV. The cross section has a very small nonzero value at zero relative translational energy. This arises from the small tunnelling contribution to the reaction probability. Except for this, the cross section shows the typical behavior for a reaction with an energy barrier along the MEP between reactants and products. Also shown in the figure are the values of the cross section at different energies evaluated by the quasiclassical trajectory method⁴⁵ for O $_2$ ($v=0, j=0$) using the TRIQCT program.⁴⁶ The agreement between the QCT and the wave packet calculations is quite satisfactory in this case showing that, as expected, there are no large quantum effects for this reaction, except perhaps in the vicinity of the threshold energy.

Table II presents calculated values of the thermal rate constant, $k(T)$, for reaction (2) on the $2^2A'$ PES. The wave packet results (WP) are calculated from the cross section data of Fig. 5(A). The table also lists the rate constants computed using the QCT and two VTST methods [ICVT (improved canonical VTST) and ICVT/ μ OMT [ICVT method including the microcanonical optimized multidimensional (μ OMT) correction to account for the tunnelling contribution to reactivity]].^{47,48} All VTST calculations have been per-

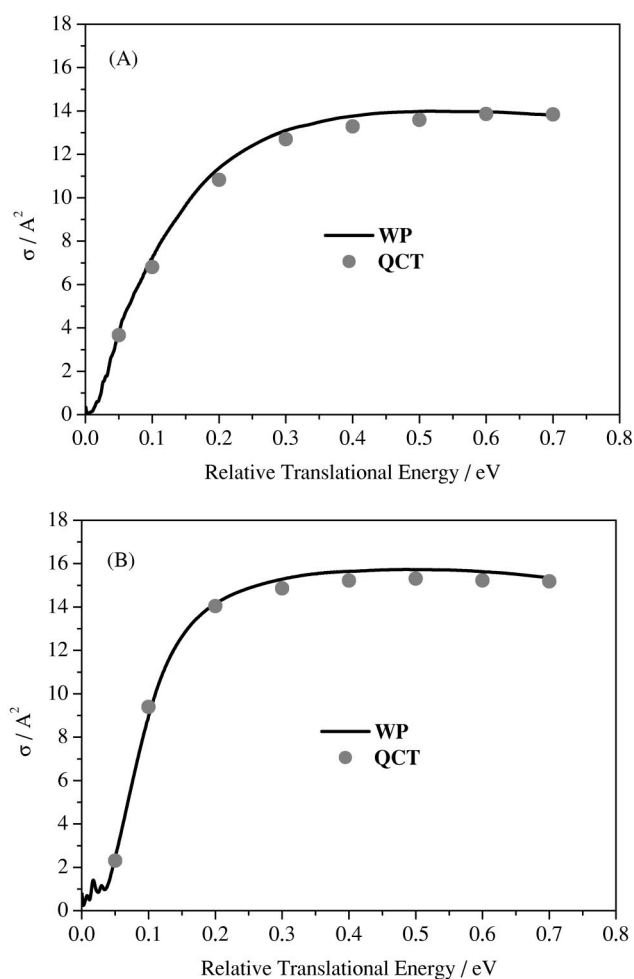


FIG. 5. Total reactive cross section, calculated using the quantum wave packet method, for the reaction $N(^2D) + O_2(X^3\Sigma_g^-) \rightarrow O(^3P) + NO(X^2\Pi)$. The initial vibrational-rotational state of the O $_2$ reactant is $v=0, j=0$. The cross sections correspond to calculations on the two lowest adiabatic potential energy surfaces and are plotted as a function of the relative translational energy E_{tr} : (A) $2^2A'$ PES and (B) $1^2A''$ PES. Also shown are quasiclassical trajectory results (shaded circles).

formed using the POLYRATE program.⁴⁷ In the case of the QCT and VTST calculations a thermal distribution of the vibrotational levels of the O $_2$ reactant is properly taken into account, while in the wave packet calculations only the O $_2$ ($v=0, j=0$) state is used. In the range of temperatures studied the agreement between different methods is, on the whole, quite good. We see that at low temperatures and at room temperature, i.e., 100–300 K, there is a considerable difference between the wave packet results and those obtained with the other methods. The difference is largest at the lowest temperatures and reduces progressively as the temperature increases. Interestingly we see that wave packet method, which accurately takes account of tunnelling and zero-point vibrational effects, yields a lower rate constant than either the QCT or the ICVT/ μ OMT methods.

The good agreement found between the wave packet and the QCT cross sections for the $2^2A'$ PES with O $_2$ ($v=0, j=0$) [see Fig. 5(A)] suggests that the cause of the disagreement between the theoretical rate constants at low temperatures (Table II) is likely to lie in the neglect of excited vibro-

TABLE II. Rate constants for reaction (2) calculated on the $2^2A'$ PES.

T (K)	$k(T)$ ($\text{cm}^3 \text{ molecule}^{-1} \text{ s}^{-1}$)			
	WP ^a	QCT	ICVT ^b	ICVT/ μ OMT ^b
100	$3.62 \cdot 10^{-12}$	$9.20 \cdot 10^{-12}$	$8.36 \cdot 10^{-12}$	$1.12 \cdot 10^{-11}$
200	$1.45 \cdot 10^{-11}$	$2.21 \cdot 10^{-11}$	$2.19 \cdot 10^{-11}$	$2.36 \cdot 10^{-11}$
300	$2.84 \cdot 10^{-11}$	$3.46 \cdot 10^{-11}$	$3.46 \cdot 10^{-11}$	$3.58 \cdot 10^{-11}$
400	$4.34 \cdot 10^{-11}$	$4.69 \cdot 10^{-11}$	$4.69 \cdot 10^{-11}$	$4.78 \cdot 10^{-11}$
500	$5.88 \cdot 10^{-11}$	$5.42 \cdot 10^{-11}$	$5.89 \cdot 10^{-11}$	$5.97 \cdot 10^{-11}$
600	$7.40 \cdot 10^{-11}$	$7.57 \cdot 10^{-11}$	$7.09 \cdot 10^{-11}$	$7.15 \cdot 10^{-11}$
700	$8.88 \cdot 10^{-11}$	$9.55 \cdot 10^{-11}$	$8.28 \cdot 10^{-11}$	$8.33 \cdot 10^{-11}$
800	$1.03 \cdot 10^{-10}$	$1.05 \cdot 10^{-10}$	$9.47 \cdot 10^{-11}$	$9.51 \cdot 10^{-11}$
900	$1.16 \cdot 10^{-10}$	$1.17 \cdot 10^{-10}$	$1.06 \cdot 10^{-10}$	$1.07 \cdot 10^{-10}$
1000	$1.28 \cdot 10^{-10}$	$1.28 \cdot 10^{-10}$	$1.18 \cdot 10^{-10}$	$1.19 \cdot 10^{-10}$

^aWP results are for $\text{O}_2(v=0, j=0)$, while thermal vibrotational distributions of O_2 were used in the QCT and VTST calculations. The VTST results have been obtained using the minimum energy path (intrinsic reaction coordinate) for abstraction. See text.

^bCalculations were performed using the POLYRATE code, Ref. 47.

tational states in the wave packet calculations. At higher temperatures, in the range between 400 and 1000 K the different calculations for the rate constant agree very well with each other. The difference between the wave packet and both the ICVT and the ICVT/ μ OMT methods^{47,48} is less than or equal to 10%. It is interesting to note that at the highest temperatures studied the wave packet calculations agree best (within 0.5%) with the QCT results, both of which yield somewhat higher rate constants in this limit than the VTST calculations.

Figure 5(B) shows the total reactive cross section for reaction (2) on the $1^2A''$ surface with O_2 initially in its ($v=0, j=0$) vibrotational state. It is qualitatively similar to the cross section for reaction on the $2^2A'$ PES. Compared with the latter cross section, the $1^2A''$ cross section increases somewhat more rapidly with increasing relative translational energy, reaching a near constant value at a collision energy of about 0.3 eV as compared with an energy of about 0.4 eV for the $2^2A'$ PES. The cross section also shows a slightly greater amount of reactivity at very low relative translational energies, indicating a greater degree of tunnelling. There is, furthermore, some residual resonance structure still present in the cross section at low energies. While the summation over many J values has decreased the magnitude of this resonance structure, it has not, in this case, entirely wiped it out. The absolute magnitude of the cross section is slightly greater than that for the $2^2A'$ PES. The figure also shows cross sections obtained using the QCT method on the same surface. The QCT results agree very well with the quantum wave packet calculations.

Table III presents the calculated thermal rate constants $k(T)$ for reaction (2) on the $1^2A''$ PES. In the case of the wave packet calculations the rate constants are calculated from the cross section of Fig. 5(B). The table also lists the rate constants computed using the QCT, ICVT,⁴⁸ and ICVT/ μ OMT (Ref. 48) methods. These latter rate constants are computed using a thermal distribution of initial O_2 vibrotational states. Again, as for the dynamics on the $2^2A'$ PES, the agreement between different methods is quite good at the higher temperatures, but much less so at the lowest tempera-

TABLE III. Rate constants for reaction (2) calculated on the $1^2A''$ PES.

T (K)	$k(T)$ ($\text{cm}^3 \text{ molecule}^{-1} \text{ s}^{-1}$)			
	WP ^a	QCT	ICVT ^b	ICVT/ μ OMT ^b
100	$4.21 \cdot 10^{-12}$	$1.10 \cdot 10^{-11}$	$9.61 \cdot 10^{-12}$	$1.20 \cdot 10^{-11}$
200	$1.28 \cdot 10^{-11}$	$3.61 \cdot 10^{-11}$	$3.20 \cdot 10^{-11}$	$3.37 \cdot 10^{-11}$
300	$2.78 \cdot 10^{-11}$	$5.62 \cdot 10^{-11}$	$5.93 \cdot 10^{-11}$	$6.07 \cdot 10^{-11}$
400	$4.61 \cdot 10^{-11}$	$7.95 \cdot 10^{-11}$	$8.84 \cdot 10^{-11}$	$8.97 \cdot 10^{-11}$
500	$6.56 \cdot 10^{-11}$	$1.01 \cdot 10^{-10}$	$1.19 \cdot 10^{-10}$	$1.20 \cdot 10^{-10}$
600	$8.50 \cdot 10^{-11}$	$1.19 \cdot 10^{-10}$	$1.50 \cdot 10^{-10}$	$1.50 \cdot 10^{-10}$
700	$1.04 \cdot 10^{-10}$	$1.38 \cdot 10^{-10}$	$1.81 \cdot 10^{-10}$	$1.81 \cdot 10^{-10}$
800	$1.21 \cdot 10^{-10}$	$1.52 \cdot 10^{-10}$	$2.12 \cdot 10^{-10}$	$2.12 \cdot 10^{-10}$
900	$1.38 \cdot 10^{-10}$	$1.70 \cdot 10^{-10}$	$2.43 \cdot 10^{-10}$	$2.43 \cdot 10^{-10}$
1000	$1.52 \cdot 10^{-10}$	$1.92 \cdot 10^{-10}$	$2.73 \cdot 10^{-10}$	$2.73 \cdot 10^{-10}$

^aWP results are for $\text{O}_2(v=0, j=0)$, while thermal vibrotational distributions of O_2 were used in the QCT and VTST calculations. The VTST results have been obtained using the minimum energy path (intrinsic reaction coordinate) for abstraction. See text.

^bCalculations were performed using the POLYRATE code, Ref. 47.

tures. The disagreement between the wave packet and the other calculations at the lower temperatures leads to the same conclusions as discussed above in connection with Table II. In this case the agreement between the different methods at high temperatures is much less good than was the case for the $2^2A'$ PES (see Table II).

Figure 1 shows that there are a total of 30 surfaces, including spin-orbit interaction, which correlate with the $\text{N}(^2D) + \text{O}_2(X^3\Sigma_g^-)$ reactants. In the present work we have taken account of reaction on the two most important doublet surfaces. Reaction on these two surfaces dominates at low and moderate temperatures.^{6,7,8} We can estimate the overall or global total reaction cross section for reaction (2) using the relationship,

$$\sigma_{\text{global}} = \frac{1}{15} \sigma_{2^2A' \text{ PES}} + \frac{1}{15} \sigma_{1^2A'' \text{ PES}}. \quad (16)$$

Figure 6 shows the comparison of the overall reactive cross section for reaction (2) with O_2 initially in its ($v=0, j=0$) vibrotational state computed using Eq. (16) with the QCT results. Two different QCT curves are shown. The curve with open circles include the reactivity on only the $2^2A'$ and $1^2A''$ PESs, while the curve with asterisks also includes reactivity arising from two extra doublet surfaces ($3^2A'$, see Ref. 9, and $2^2A''$, see Ref. 49) which also correlate adiabatically between reactants and products for reaction (2). As in the case of Figs. 5(A) and 5(B) we see that the agreement between the wave packet and the QCT cross sections is very good. The deviation at larger reactant relative translational energies between the wave packet and the four surface QCT calculations (*) is entirely due to the inclusion of the contribution from the two additional PESs (Refs. 9, 49) in the latter case. These additional surfaces contribute only at higher energies.

Table IV presents the calculated and experimental¹⁰ global thermal rate constants. For the wave packet calculations these are computed from the cross sections shown in Fig. 6. The QCT and the ICVT/ μ OMT results include contributions from two extra PESs as compared with the wave packet calculations and also take into account the thermal distribution

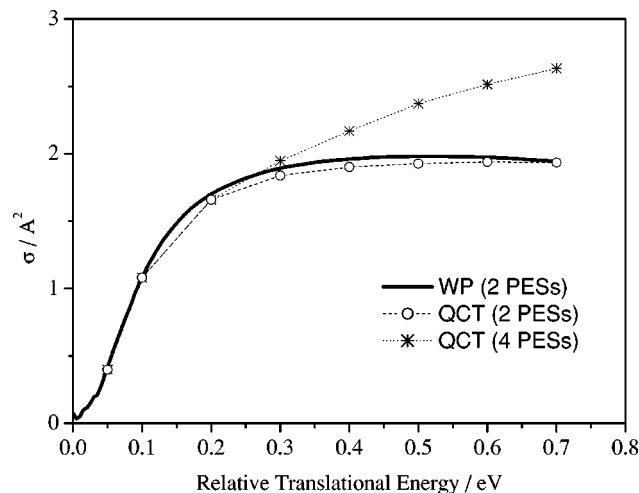


FIG. 6. Overall total reactive cross section for the reaction $\text{N}(\text{}^2D) + \text{O}_2(\text{}^3\Sigma_g^-) \rightarrow \text{O}(\text{}^3P) + \text{NO}(\text{}^2\Pi)$, calculated using the quantum wave packet method. The initial vibrational-rotational state of the O_2 reactant is $v=0, j=0$. The cross sections have been summed over contributions from both the $2\text{}^2A'$ and $1\text{}^2A''$ potential energy surfaces [see Eq. (16)] and are plotted as a function of the collision energy E_{tr} (continuous line). Also shown are the results of two different quasiclassical trajectory calculations. The open circles show the results of QCT calculations in which reaction occurs on the same two PESs as used in the wave packet calculations, while the asterisks show the QCT results taking into account the additional two excited PESs, as discussed in the text.

of O_2 initial quantum states. The QCT and ICVT/ μ OMT results are consistently higher than the wave packet results, but are completely in line with the results obtained for the two separate surfaces (see Tables II and III). The contribution of the two extra potential energy surfaces to the rate constant is very small (3%) even at the highest temperatures studied

The experimental results correspond to the rate of disappearance of $\text{N}(\text{}^2D)$ and include “physical electronic quench-

ing” as well as reaction as a destruction mechanism. The experimentally measured rate constants should therefore be an upper limit to the calculated global reaction rate constant. The ICVT/ μ OMT rate constants for temperatures 200–400 K listed in Table IV are all greater than the listed experimentally values. No firm conclusion can be drawn from this discrepancy, as the experimental results are associated with a substantial uncertainty and the range of this uncertainty encompasses the QCT and the ICVT/ μ OMT predicted values (see Ref. 10). The wave packet estimate of the rate constant at 200 K, on the other hand, seems to be too low as compared with the experimental value; this may be due to the fact that the wavepacket calculations have not included a proper averaging over the thermal distribution of initial quantum states.

V. CONCLUSIONS

Quantum scattering calculations have been performed for the total reaction probabilities of the $\text{N}(\text{}^2D) + \text{O}_2(\text{}^3\Sigma_g^-) \rightarrow \text{O}(\text{}^3P) + \text{NO}(\text{}^2\Pi)$ reaction on the two lowest potential energy surfaces involved ($2\text{}^2A'$ and $1\text{}^2A''$ PESs) and for many values of the total angular momentum quantum number, J . The time-dependent real wave packet approach²³ has been used in all the calculations and the resulting total reaction probabilities display some intriguing features, namely, a stepped structure in the energy dependence of the reaction probability for the $2\text{}^2A'$ potential energy surface [see Fig. 4(A)] and three clear well characterized resonance features for reactive scattering on the $1\text{}^2A''$ surface [see Fig. 4(B)]. Even more interesting is the fact that the first of these features occurs in the low energy tunnelling region of the energy spectrum. The $J=0$ quantum reactive probabilities for both PESs show marked resonance features [see Figs. 3(A) and 3(B)]. This resonance structure vanishes as the total angular momentum, J , is increased [see Figs. 4(A) and 4(B)]. The reaction probability predicted using the wave packet method is nonzero at total energies below that of the transition state barrier (including zero-point vibrational energy) for both PESs. This indicates that the wave packet method does predict the existence of some tunnelling.

The computed quantum wave packet reaction probabilities for a large number of J values have been used, in conjunction with a capture model approach, to estimate total cross sections for the reaction. These reaction cross sections have been compared with the reaction cross sections computed using the quasiclassical trajectory method. In general remarkably good agreement is observed between the QCT and wave packet cross sections. Further investigation is required to investigate whether this agreement persists even at very low collision energies, for which we do not currently have the QCT results. In both the wave packet and QCT calculations the initial quantum state of the O_2 was the lowest vibrotational level $\text{O}_2(v=0, j=0)$. The summation over total angular momentum required to compute the cross section from the J dependent reaction probabilities greatly reduces the resonance structure, but for the $1\text{}^2A''$ PES a small part of this structure survives in the total reactive cross section [see Fig. 5(B)].

TABLE IV. Rate constants for reaction (2)

T (K)	$k(T)$ ($\text{cm}^3 \text{ molecule}^{-1} \text{ s}^{-1}$)			
	WP ^a	QCT	ICVT/ μ OMT ^b	Experimental ^c
100	$5.16 \cdot 10^{-13}$	$(1.41 \pm 0.12) \cdot 10^{-12}$	$1.62 \cdot 10^{-12}$	
200	$1.82 \cdot 10^{-12}$	$(4.02 \pm 0.13) \cdot 10^{-12}$	$3.91 \cdot 10^{-12}$	$3.85 \cdot 10^{-12}$
300	$3.75 \cdot 10^{-12}$	$(6.13 \pm 0.10) \cdot 10^{-12}$	$6.54 \cdot 10^{-12}$	$5.24 \cdot 10^{-12}$
400	$5.98 \cdot 10^{-12}$	$(8.43 \pm 0.23) \cdot 10^{-12}$	$9.29 \cdot 10^{-12}$	$6.11 \cdot 10^{-12}$
500	$8.30 \cdot 10^{-12}$	$(1.04 \pm 0.02) \cdot 10^{-11}$	$1.22 \cdot 10^{-11}$	
600	$1.06 \cdot 10^{-11}$	$(1.31 \pm 0.03) \cdot 10^{-11}$	$1.50 \cdot 10^{-11}$	
700	$1.28 \cdot 10^{-11}$	$(1.57 \pm 0.03) \cdot 10^{-11}$	$1.79 \cdot 10^{-11}$	
800	$1.50 \cdot 10^{-11}$	$(1.74 \pm 0.04) \cdot 10^{-11}$	$2.09 \cdot 10^{-11}$	
900	$1.69 \cdot 10^{-11}$	$(1.95 \pm 0.04) \cdot 10^{-11}$	$2.39 \cdot 10^{-11}$	
1000	$1.87 \cdot 10^{-11}$	$(2.23 \pm 0.03) \cdot 10^{-11}$	$2.70 \cdot 10^{-11}$	

^aWP results are for $\text{O}_2(v=0, j=0)$, while thermal vibrotational distributions of O_2 were used in the QCT and VTST calculations. The VTST results have been obtained using the minimum energy path (intrinsic reaction coordinate) for abstraction. See text.

^bCalculations were performed using the POLYRATE code, Ref. 47.

^cIncluding both reactive channels [reactions (1) and (2)] and the physical electronic quenching of $\text{N}(\text{}^2D)$ (Ref. 10). This reference gives the error estimate for the rate constant as $k(298 \text{ K}) = 5.2(+1.6, -1.2) \cdot 10^{-12} \text{ cm}^3 \text{ molecule}^{-1} \text{ s}^{-1}$. Experimental error margins are larger at lower and higher temperatures.

The quantum mechanical cross sections have been used to compute total rate constants for the reaction and have then been compared with rate constants computed using the QCT (Refs. 45, 46) and VTST (ICVT and ICVT/ μ OMT) (Refs. 47, 48) methods on the same potential energy surfaces, and also with experimental results.¹⁰ In these comparisons both the QCT and VTST results assumed a thermal distribution of vibrotational levels of O₂. The comparisons are on the whole quite good. The QCT and VTST methods predict rate constants that are consistently higher than those predicted by the wave packet calculations at low to room temperatures (100–300 K). This difference is likely, in part, to arise from the use of only the O₂($v=0, j=0$) level as the initial state in the wave packet calculations. The difference between the wave packet and the QCT rate constants diminishes as the temperature increases. For the 2²A' PES the two agree almost perfectly at 800 K. For reaction on the 1²A'' PES the wave packet and QCT results do not agree to the same extent at high temperatures. The disagreement between the QCT and VTST rate constants for this surface at high temperatures may be understood on the basis that the VTST calculations consider the minimum energy path (intrinsic reaction coordinate) of the abstraction pathway, while in the case of the quasiclassical trajectories the system can evolve towards products following both abstraction and insertion pathways.

The global total reaction rate constant for the wave packet calculations is estimated by combining the rate constants arising from reaction on the two potential energy surfaces considered. Reaction on these two surfaces has been shown to constitute the main contribution to the rate of reaction, especially at low and moderate temperatures.^{6–8} These global rate constants have been compared with ones computed using the QCT and ICVT/ μ OMT methods and with experiment.¹⁰ The global rate constants calculated using the QCT and ICVT/ μ OMT methods (see Table IV) include contributions from reaction on two other potential energy surfaces (3²A' and 2²A'') and also take account of the thermal distribution of the O₂ vibrotational states. The contribution from the two extra potential energy surfaces amounts at most to 3% of the rate constants in the energy range examined. At first glance the QCT and ICVT/ μ OMT methods appear to somewhat overestimate the reaction rate as compared with the experimental values (see Table IV), but the values fall within the experimental uncertainty. As the experiments measure the rate of disappearance of the N(²D) reactant and include a contribution from nonreactive physical electronical de-excitation, they represent an upper bound to the calculated rate constants. The fact that the current wave packet calculations yield a lower value for the rate constants is in part due to the exclusive use of the lowest vibrotational state of O₂ as the initial state in these calculations.

As indicated above, the present wave packet calculations are all based on reactants initially in their ground vibrational-rotational states ($v=0, j=0$), and the dependence of the reaction probabilities and other properties on the initial reactant quantum states still remains to be investigated.

ACKNOWLEDGMENTS

The authors I.M., M.G., and R.S. thank the Spanish Ministry of Education and Culture (DGES Project Ref. No. PB98-1209-C02-01). Financial support from the European Union (INTAS Project Ref. No. 99-00701) and the "Generalitat de Catalunya" (Autonomous Government of Catalonia) (Projects Refs. Nos. 2000SGR 00016 and 2001SGR 00041) is acknowledged. I.M. is also grateful to the "Generalitat de Catalunya" for a predoctoral research grant. G.G.B.K. thanks the EPSRC for the provision of funds to purchase the computer equipment on which these calculations were performed. S.K.G. was supported by the Office of Basic Energy Sciences, Division of Chemical Sciences, U.S. Department of Energy, under Contract No. W-31-109-ENG-38. E.M.G. acknowledges support of this research from NSF Grant No. CHE-9970994.

- ¹Y. Shihira, T. Suzuki, S. Unayuma, H. Umemoto, and S. Tsunashima, J. Chem. Soc., Faraday Trans. **90**, 549 (1994).
- ²M. W. Chase, Jr., C. A. Davies, J. R. Downey, Jr., D. J. Frurip, R. A. McDonald, and A. N. Syverud, J. Phys. Chem. Ref. Data Suppl. **1**, 14 (1985).
- ³S. Baskin and J. A. Stanner, in *Atomic Energy Levels and Grottrian Diagrams 1* (North-Holland, Amsterdam, 1975), Vol. 1.
- ⁴L. E. Jusinski, G. Black, and T. G. Slanger, J. Phys. Chem. **92**, 5977 (1988).
- ⁵M. Braunstein and J. W. Duff, J. Chem. Phys. **113**, 7406 (2000).
- ⁶M. González, I. Miquel, and R. Sayós, Chem. Phys. Lett. **335**, 339 (2001).
- ⁷M. González, I. Miquel, and R. Sayós, J. Chem. Phys. **115**, 2530 (2001).
- ⁸M. González, I. Miquel, and R. Sayós, J. Chem. Phys. **115**, 8838 (2001).
- ⁹M. González, I. Miquel, and R. Sayós, Chem. Phys. Lett. **360**, 521 (2002).
- ¹⁰J. T. Herron, J. Phys. Chem. Ref. Data **28**, 1453 (1999).
- ¹¹W. T. Rawlins, M. E. Fraser, and S. M. Miller, J. Phys. Chem. **93**, 1097 (1989).
- ¹²R. J. Donovan and D. Hussain, Chem. Rev. **70**, 489 (1970).
- ¹³M. Gilibert, A. Aguilar, M. González, and R. Sayós, Chem. Phys. **172**, 99 (1993).
- ¹⁴M. Gilibert, A. Aguilar, M. González, and R. Sayós, Chem. Phys. **178**, 178 (1993).
- ¹⁵R. Sayós, A. Aguilar, M. Gilibert, and M. González, J. Chem. Soc., Faraday Trans. **89**, 3223 (1993).
- ¹⁶M. Gilibert, X. Giménez, M. González, R. Sayós, and A. Aguilar, Chem. Phys. **191**, 1 (1995).
- ¹⁷R. Sayós, J. Hijazo, M. Gilibert, and M. González, Chem. Phys. Lett. **284**, 101 (1998).
- ¹⁸P. Defazio, C. Petrongolo, S. K. Gray, and C. Oliva, J. Chem. Phys. **115**, 3208 (2001).
- ¹⁹D. Reignier, T. Stoecklin, P. Halvick, A. Voronin, and J. C. Rayez, Phys. Chem. Chem. Phys. **3**, 2726 (2001).
- ²⁰K. S. Sorbie and J. N. Murrell, Mol. Phys. **31**, 905 (1976).
- ²¹J. N. Murrell, S. Carter, S. C. Farantos, P. Huxley, and A. J. C. Varandas, *Molecular Potential Energy Functions* (Wiley, Chichester, 1984).
- ²²M. González, C. Oliva, and R. Sayós, J. Chem. Phys. **117**, 680 (2002).
- ²³S. K. Gray and G. G. Balint-Kurti, J. Chem. Phys. **108**, 950 (1998).
- ²⁴S. K. Gray and E. M. Goldfield, J. Chem. Phys. **115**, 8331 (2001).
- ²⁵G. G. Balint-Kurti, *Lecture Notes in Chemistry*, edited by A. Laganà and A. Riganelli (Springer Verlag, Berlin, 2000), Vol. 75, p. 74.
- ²⁶J. V. Lill, G. A. Parker, and J. C. Light, Chem. Phys. Lett. **89**, 483 (1982).
- ²⁷J. V. Lill, G. A. Parker, and J. C. Light, J. Chem. Phys. **85**, 900 (1986).
- ²⁸M. Hankel and G. G. Balint-Kurti, J. Chem. Phys. **113**, 9658 (2000).
- ²⁹V. Piermarini, G. G. Balint-Kurti, S. K. Gray, F. Gögtas, A. Laganà, and M. L. Hernández, J. Phys. Chem. A **105**, 5743 (2001).
- ³⁰V. A. Mandelshtam and H. S. Taylor, J. Chem. Phys. **102**, 7390 (1995).
- ³¹V. A. Mandelshtam and H. S. Taylor, J. Chem. Phys. **103**, 2903 (1995).
- ³²Y. Huang, D. J. Kouri, and D. K. Hoffman, J. Chem. Phys. **101**, 10493 (1994).

- ³³Y. Huang, S. S. Iyengar, D. J. Kouri, and D. K. Hoffman, J. Chem. Phys. **105**, 927 (1996).
- ³⁴Á. Vibók and G. G. Balint-Kurti, J. Chem. Phys. **96**, 7615 (1992).
- ³⁵Á. Vibók and G. G. Balint-Kurti, J. Phys. Chem. **96**, 8712 (1992).
- ³⁶G. G. Balint-Kurti, A. I. Gonzalez, E. M. Goldfield, and S. K. Gray, Faraday Discuss. **110**, 169 (1998).
- ³⁷A. J. H. M. Meijer, E. M. Goldfield, S. K. Gray, and G. G. Balint-Kurti, Chem. Phys. Lett. **293**, 270 (1998).
- ³⁸G. G. Balint-Kurti, in *International Review-of-Science, Series II*, edited by A. D. Buckingham and C. A. Coulson (Butterworths, London, 1975), Vol. 4, p. 286.
- ³⁹G. C. Schatz and A. Kuppermann, J. Chem. Phys. **65**, 4642 (1976).
- ⁴⁰S. K. Gray, E. M. Goldfield, G. C. Schatz, and G. G. Balint-Kurti, Phys. Chem. Chem. Phys. **1**, 1141 (1999).
- ⁴¹J. M. Bowman, J. Phys. Chem. **95**, 4960 (1991).
- ⁴²S. K. Gray, G. G. Balint-Kurti, G. C. Schatz, J. J. Lin, X. Liu, S. Harich, and X. Yang, J. Chem. Phys. **113**, 7330 (2000).
- ⁴³E. M. Goldfield and A. J. H. M. Meijer, J. Chem. Phys. **113**, 11055 (2000).
- ⁴⁴A. J. H. M. Meijer and E. M. Goldfield, Phys. Chem. Chem. Phys. **3**, 2811 (2001).
- ⁴⁵H. R. Mayne, Int. Rev. Phys. Chem. **10**, 107 (1991).
- ⁴⁶R. Sayós and M. González, TRIQCT (unpublished program).
- ⁴⁷R. Stecker, Y. Chuang, E. L. Coitino, *et al.*, POLYRATE (Version 7.0), D. G. Truhlar, Department of Chemistry and Supercomputer Institute, University of Minnesota, Minneapolis, MN 55455 (1996).
- ⁴⁸T. Allison and D. G. Truhlar, in *Modern Methods for Multidimensional Dynamics Computations in Chemistry*, edited by D. L. Thompson (World Scientific, Singapore, 1998).
- ⁴⁹I. Miquel, Ph.D. thesis, University of Barcelona, 2002.